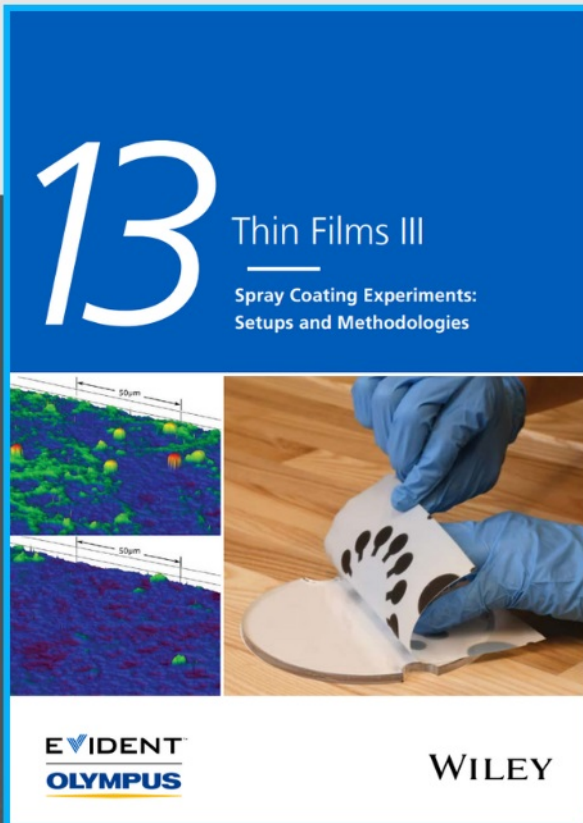




# Spray Coating Experiments: Setups and Methodologies



**The latest eBook from  
Advanced Optical Metrology.  
Download for free.**

*Spray Coating Experiments: Setups and Methodologies*, is the third in our Thin Films eBook series. This publication provides an introduction to spray coating, three article digests from Wiley Online Library and the latest news about Evident's Image of the Year Award 2022.

Wiley in collaboration with Evident, are committed to bridging the gap between fundamental research and industrial applications in the field of optical metrology. We strive to do this by collecting and organizing existing information, making it more accessible and useful for researchers and practitioners alike.

**EVIDENT**  
**OLYMPUS**

**WILEY**

# Enhanced Thermoelectric Performance of Rare-Earth-Free n-Type Oxide Perovskite Composite with Graphene Analogous 2D MXene

Pragya Dixit, Subhra Sourav Jana, and Tanmoy Maiti\*

Here, the first experimental demonstration on the effect of incorporating new generation 2D material, MXene, on the thermoelectric performance of rare-earth-free oxide perovskite is reported. The charge localization phenomenon is predominant in the electron transport of doped SrTiO<sub>3</sub> perovskites, which deters from achieving a higher thermoelectric power factor in these oxides. In this work, it is shown that incorporating Ti<sub>3</sub>C<sub>2</sub>T<sub>x</sub> MXene in a matrix of SrTi<sub>0.85</sub>Nb<sub>0.15</sub>O<sub>3</sub> (STN) facilitates the delocalization of electrons resulting in better than single-crystal-like electron mobility in polycrystalline composites. A 1851% increase in electrical conductivity and a 1000% enhancement in power factor are attained. Besides, anharmonicity caused by MXene in the STN matrix has led to enhanced Umklapp scattering giving rise to lower lattice thermal conductivity. Hence, 700% ZT enhancement is achieved in this composite. Further, a prototype of thermoelectric generator (TEG) using only n-type STN + MXene is fabricated and a power output of 38 mW is obtained, which is higher than the reported values for oxide TEG.

## 1. Introduction


Increased demand for energy consumption has led to the depletion of fossil fuels at the fastest possible rate. On the other hand, almost 60% of the energy consumed by manufacturing industries, power plants, and combustion engines gets wasted as heat.<sup>[1–3]</sup> Hence, developing environmentally friendly technologies that efficiently utilize waste heat to generate electricity is imperative. A thermoelectric generator (TEG), capable of converting waste heat into electricity, is one of the most promising devices to cope with the power generation crisis without leaving behind any carbon footprint. The efficiency of TEG is determined by the figure of merit,  $ZT = S^2\sigma T/\kappa$ ; where  $S$  is the Seebeck coefficient,  $\sigma$  is the electrical conductivity,  $T$  is the temperature, and  $\kappa$  is the thermal conductivity. We need a high  $S^2\sigma$  (power factor) and a small  $\kappa$  value to get a high  $ZT$ , which is challenging since the inherent conflict persists among the

constituent parameters. Among the available classes of thermoelectric materials, narrow-band gap chalcogenides<sup>[4]</sup> have shown high  $ZT$ . But these metal chalcogenides serve the purpose only in the low-temperature range. For large-scale power generation using high-grade heat, we need a material that is earth-abundant, nontoxic, and physically, chemically, and thermally stable near 1000 °C. From that perspective, oxides are promising candidates for high-temperature thermoelectric power generation. Among the bulk, n-type oxide thermoelectric materials, donor-doped SrTiO<sub>3</sub> (STO) have shown the best thermoelectric performance with  $ZT = 0.6$ .<sup>[5]</sup> However,  $ZT > 1$  is a prerequisite for practical applications, which has been challenging to achieve in doped STO bulk oxides. The reasons behind their poor  $ZT$  values are their high thermal

conductivity and poor electrical conductivity. It is observed that doping alone cannot improve the transport properties of STO. One must decouple the power factor ( $S^2\sigma$ ) and lattice thermal conductivity ( $\kappa_l$ ) to attain high  $ZT$  values. Grain boundary engineering<sup>[6,7]</sup> and nanocompositing<sup>[8–22]</sup> are some of the viable routes to enhance both electron transport and induce more phonon scattering in bulk oxides.

Incorporating graphite,<sup>[8,9]</sup> graphene oxide,<sup>[10]</sup> and graphene<sup>[19,22]</sup> into the donor (La, Nb)-doped STO matrix have significantly improved the  $ZT$  of STO-based bulk oxides. The most profound aspect of  $ZT$  enhancement in doped STO systems reported by various researchers is the single-crystal-like<sup>[9,19,23]</sup> electron mobility attained in these polycrystalline ceramics when they have formed composites with carbon derivatives. However, the reasons behind such huge surge in electron mobility leading to a manifold increase in electrical conductivity are yet to be fully understood. In STO-based composites with 2D graphene, enhanced electron transport is attributed to the reduction of Schottky barrier height in polycrystalline-doped STO.<sup>[11,19]</sup> However, it is debatable whether reducing the Schottky barrier alone can cause single-crystal-like electron mobility in doped STO-based composites.<sup>[23,24]</sup> Formation of the Schottky barrier is usual phenomena observed in polycrystalline materials and the presence of 2D graphene along the grain boundaries<sup>[11]</sup> is expected to facilitate the formation of excess oxygen vacancies enabling the reduction of Schottky barrier height. But that should not be specific to a particular

P. Dixit, S. S. Jana, T. Maiti  
Plasmonics and Perovskites Laboratory  
Department of Materials Science and Engineering  
IIT Kanpur  
Kanpur, Uttar Pradesh 208016, India  
E-mail: tmaiti@iitk.ac.in

 The ORCID identification number(s) for the author(s) of this article can be found under <https://doi.org/10.1002/smll.202206710>.

DOI: 10.1002/smll.202206710

material (doped STO). Rahman et al.<sup>[11]</sup> first used the concept of Schottky barrier reduction to enhance the electrical conductivity of undoped STO by making a composite with reduced graphene oxide (r-GO). They reported enhancement of both carrier concentration and mobility in STO+r-GO composites along with the reduction in the Seebeck coefficient, which is expected from the Schottky barrier model. Likewise, the incorporation of graphene in simple transition metal oxide like TiO<sub>2</sub><sup>[18]</sup> could enhance the electrical conductivity manifold but at the expense of a monotonically decrease in the Seebeck coefficient. However, the researchers achieved the increase in electrical conductivity of the donor (La or/and Nb)-doped STO with graphene<sup>[11,12,22]</sup> with little change in the Seebeck coefficient. Moreover, the metal-like behavior ( $d\sigma/dT < 0$ ) is observed in temperature-dependent Seebeck coefficient measurement of doped STO + graphene composites, although their electrical conductivity shows a transition from thermally activated semiconductor ( $d\sigma/dT > 0$ ) to metal ( $d\sigma/dT < 0$ ) transition, unlike the undoped STO-based composites.<sup>[11]</sup> Schottky barrier model fails to explain these anomalies in charge transport found among the graphene-based composites of TiO<sub>2</sub>,<sup>[18]</sup> undoped STO,<sup>[11,21]</sup> and donor-doped STO.<sup>[12,19]</sup> Further, researchers have shown a 250 times increase in electrical conductivity of Nb-doped STO, resulting in an improvement of ZT by 50 times<sup>[10]</sup> when graphene oxide (GO) is incorporated in a doped STO matrix. GO is relatively insulator in nature compared to highly conductive graphene and is not expected to create a graphene-like reducing atmosphere near the STO grains, which rules out the Schottky barrier model for explaining the enhanced electron transport observed in the doped STO system. Recently, researchers<sup>[8,9]</sup> have shown that the incorporation of graphite as nanoinclusion and nanograins in the doped STO matrix helps achieve better electron mobility than single-crystal of doped STO giving rise to highest ever ZT of 1.42 recorded in bulk oxide. Unlike 2D graphene, which modifies the grain boundaries of STO,<sup>[12,19]</sup> graphite tends to form separate grains, which is unlikely to cause a similar effect like graphene in reducing Schottky barrier height in polycrystalline ceramics. Interestingly, researchers still managed to enhance the electrical conductivity by 46 times without much effect on Seebeck coefficient in graphite-based composites with Nb-doped STO. In order to understand the reason behind single-crystal-like electron mobility and electrical conductivity of doped STO-based composites, one should look into the reason behind oppressed conductivity observed in doped STO in spite of possessing high electron concentration ( $10^{19}$ – $10^{21}$  cm<sup>-3</sup>), which typically satisfies the Mott's criteria<sup>[25]</sup> for semiconductor to metal transition. In complex oxides like donor-doped STO, where the carrier localization phenomena persist due to the presence of multivalent cations and omnipresent oxygen vacancies in the system, simple band-model may not be appropriate to elucidate the charge transport mechanism. Variation of local electric field and strain is expected in these complex oxides, which causes the Anderson localization of electron in complex perovskites.<sup>[26–30]</sup> It is plausible that presence of carbon derivative in the matrix of doped STO imparts enough strain and infuses high momentum electrons, which facilitates the Anderson localized electrons to attain the itinerant state above the mobility edge. In order to further bolster this hypothesis, we have introduced 2D MXene in the matrix

of Nb-doped SrTiO<sub>3</sub>. In the recent years, MXene has evolved as an emerging 2D material due to its different functional properties.<sup>[31–39]</sup> Only couple of literature is available on MXene-doped bulk thermoelectric composites.<sup>[40,41]</sup> Lu et al.<sup>[41]</sup> have reported the effect of MXene incorporation in (Bi Sb)<sub>2</sub>Te<sub>3</sub> matrix demonstrating improved power factor and greatly reduced thermal conductivity resulted in ZT value of 1.3 at 400 K. Guo et al.<sup>[40]</sup> have reported the effect of cold sintering on the MXene-doped ZnO and showed an increased power factor value with the increased fraction of MXene. However, they did not report thermal transport properties and ZT values of oxide thermoelectrics. To the best of our knowledge, no other report has discussed the effect of 2D MXene on the overall thermoelectric performance of bulk oxides.

In the present work, we have introduced Ti<sub>3</sub>C<sub>2</sub>T<sub>x</sub> (where T<sub>x</sub>: -O, -OH, -F functional groups) MXene in the matrix of SrTi<sub>0.85</sub>Nb<sub>0.15</sub>O<sub>3</sub> (STN). Ti-based MXene is expected to create a favorable chemical environment for charge transfer in the matrix of doped STO. We are incorporating highly conductive 2D Ti<sub>3</sub>C<sub>2</sub>T<sub>x</sub> MXene with a larger lattice constant than graphite should create sufficient strain and provide high energy electrons in the STN matrix required for exciting the Anderson localized electrons to the itinerant state. Composites of SrTi<sub>0.85</sub>Nb<sub>0.15</sub>O<sub>3</sub> with Ti<sub>3</sub>C<sub>2</sub>T<sub>x</sub> MXene were synthesized using a fast-sintering technique like spark plasma sintering (SPS). We have observed that MXene incorporation indeed helps lower the semiconductor-to-metal transition temperature of STN, similar to what has been reported in rare earth nickelates,<sup>[42]</sup> promoting delocalization of electrons that help attain a 1851% increase in electrical conductivity. Further, we have fabricated a prototype of a four-legged thermoelectric power generator or TEG device comprising only n-type STN + MXene composites. TEG made of these novel composites exhibits twice the power output than that ever reported for the oxide TEGs.<sup>[9,43–48]</sup>

## 2. Results and Discussion

### 2.1. Phase and Microstructure Analysis

X-ray diffraction (XRD) data confirm the formation of a single-phase solid solution of SrTi<sub>0.85</sub>Nb<sub>0.15</sub>O<sub>3</sub> (STN), as shown in Figure 1a. The crystal structure of STN is found to be cubic with  $pm\bar{3}m$  space group using the Rietveld refinement method by FullProf program, as shown in Figure 1b and Table S1 (Supporting Information). The incorporation of Ti<sub>3</sub>C<sub>2</sub>T<sub>x</sub> MXene in STN does not change the cubic perovskite structure of STN, and the lattice parameter, as shown in Table S2 (Supporting Information), remained unchanged with Ti<sub>3</sub>C<sub>2</sub>T<sub>x</sub> MXene incorporation in the STN matrix. Also, we have not observed any XRD peak corresponding to Ti<sub>3</sub>AlC<sub>2</sub> MXene, probably due to its smaller fraction in the matrix.

However, Ti<sub>3</sub>AlC<sub>2</sub> MXene in the STN matrix has been detected by Raman spectra, as shown in Figure 1c. The appearance of the D-band around 1347 cm<sup>-1</sup> represents the disorders present in the MXene. G-band around 1593 cm<sup>-1</sup> corresponds to the stretched C–C bonds in MXene and has also been detected in all the compositions. A broader and low-intensity 2D-band around 2692 cm<sup>-1</sup> is also seen in all the compositions, implying

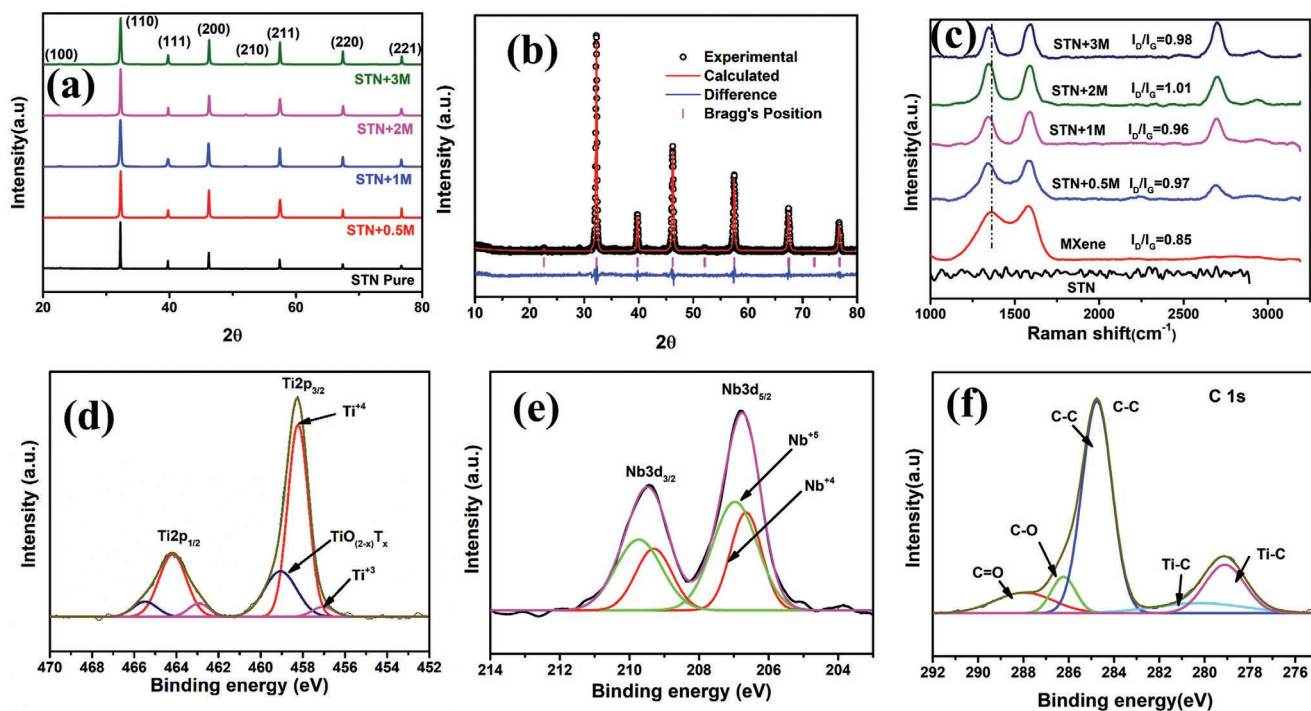


**Figure 1.** Phase and microstructure analysis: a) XRD plot for the sintered composition of STN +  $x$  wt% MXene ( $0 \leq x \leq 3$ ). b) Rietveld refinement of STN + 1 wt% MXene composite. c) Raman spectra for STN, MXene, and sintered STN + MXene composites. d–f) XPS spectra for Ti 2p, Nb 3d, and C 1s in STN + 1 wt% MXene composite, respectively.

increased disintegration of MXene layers in composites. However, it is to be noted that the D and G bands of the composites are red-shifted compared to pure MXene. That shifting occurs probably because more -O functional groups have been annexed to the MXene sheets.

Further, to confirm the elemental composition, chemical state, and functional groups of MXene, X-ray photoelectron spectroscopy (XPS) has been carried out. The fitted XPS spectra of Ti 2p, Nb 3d, and C 1s are displayed in Figure 1d–f. The binding energies, chemical states, and other functional groups formed in the composites are shown in Table S3 (Supporting Information). Ti 2p spectra, as shown in Figure 1d, show that Ti is present in both the  $Ti^{+4}$  and  $Ti^{+3}$  oxidation states, as reported in the literature.<sup>[10]</sup> However, the  $Ti^{+4}$  has a significant portion (70%), and the addition of MXene has little effect on the oxidation states of Ti. The majority of Nb is found to possess a  $Nb^{+5}$  state (60%), and the rest occupies a  $Nb^{+4}$  valence state, as shown by Nb 3d spectra in Figure 1e. According to the C 1s spectra in Figure 1f, 61% of the carbon has been found to form a C–C bond, just like in pure MXene.<sup>[49]</sup> Besides that, 8.3% and 11.4% of C have been found to form C–O and hydroxyl C=O bonds, respectively. XPS signal at 279 eV binding energy corresponds to Ti–C.

Field-emission scanning electron microscope (FESEM) image of  $Ti_3C_2T_x$  MXene, shown in Figure 2a, depicts the accordion-like layered structure of as-synthesized  $Ti_3C_2T_x$  MXene. The fractured surface of the STN + MXene composite sample further confirms the formation of dense microstructure with layered MXene, as shown in Figure 2b. Elemental color mapping carried out by energy-dispersive X-ray spectroscopy

(EDXS) shows the presence of MXene in the composite samples, as shown by black patches in Figure S1 (Supporting Information). These black patches are Ti-rich and devoid of Sr, which is evident from the EDXS mapping. The uniform distribution of C suggests that MXene is evenly dispersed in the STN matrix. Further, the distribution of MXene sheets in the STN matrix has been estimated using an electron back-scattered diffraction (EBSD) study. EBSD images, as shown in Figure 2c and Figure S2 (Supporting Information), confirm that layered MXene is forming small pockets in the matrix, which eventually aid in electronic charge conduction.

Further, the use of nanomilled STN powder and fast sintering techniques like SPS in processing the composites resulted in a wide range of grain size distribution. The bar chart in Figure 2d shows that  $\approx 25\%$  of grains are  $< 300$  nm in size, which increases the number of grain boundary interfaces and causes phonon–phonon scattering in the polycrystalline structure.<sup>[50]</sup> The presence of several micron-size ( $< 1 \mu m$ ) grains can also be observed in Figure 2c,d. These interconnected bigger grains provide a pathway for effective charge carrier conduction and help in increasing the electrical conductivity of the system. However, the presence of nanosize grains aid in reducing the lattice thermal conductivity of the composite system. Transmission electron microscope (TEM) images of sintered STN + MXene composites in Figure 2e and Figure S3 (Supporting Information) demonstrate that MXene is surrounded by STN grains, although the size of MXene is found to be at nm to  $\mu m$  level. The selected area electron diffraction (SAED) pattern shown in the inset of Figure 2e illustrates a hexagonal pattern of MXene. Figure 2f illustrates the IFFT pattern of sintered

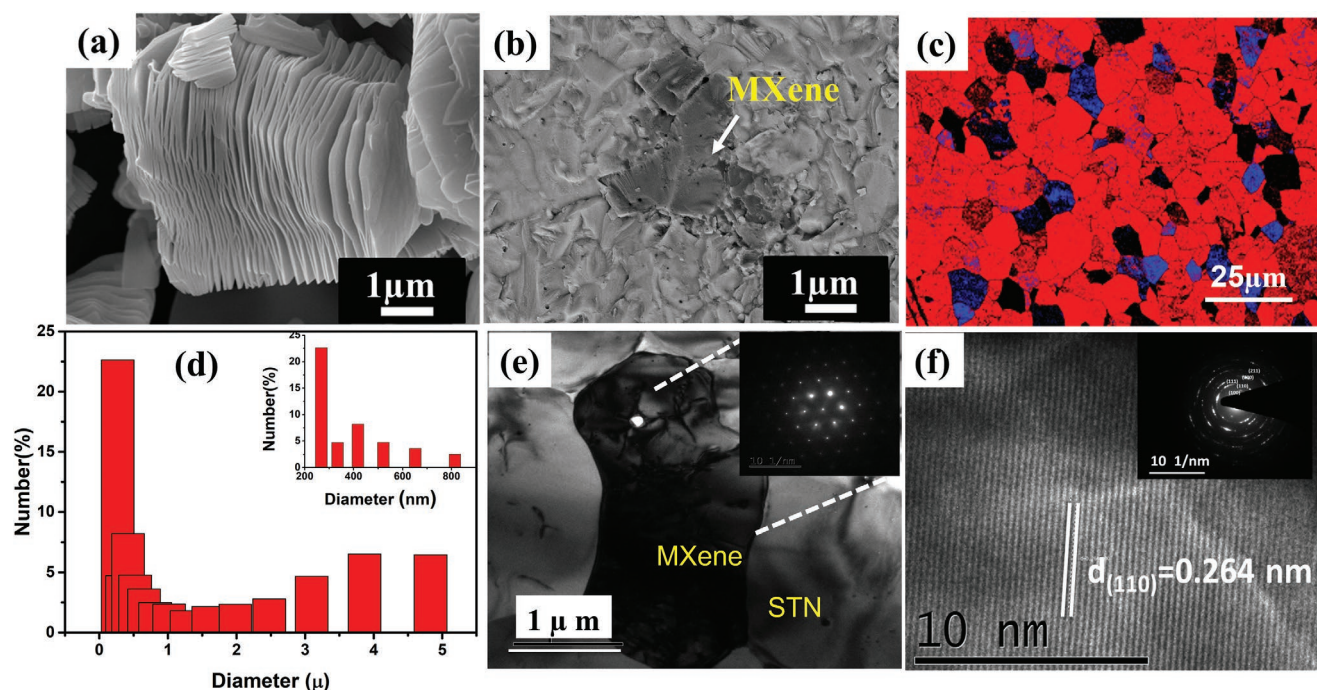


**Figure 2.** FESEM images of a) MXene showing the open layered structure. b) Fractured surface of sintered STN + 3 wt% MXene composite. c) Phase contrast image of composite with blue color pockets showing MXene and red color region representing STN. d) Grain size distribution obtained from EBSD microstructure. e) TEM image of STN + 1 wt% MXene. f) Inverse fast Fourier transformation (IFFT) image of STN + 1 wt% MXene composite illustrating spacing between two lattice fringes, inset showing the SAED ring pattern for polycrystalline sample.

powder sample, and the distance between the lattice fringes is in good agreement with the d-spacing value determined from XRD data for the cubic STN perovskite phase. The polycrystalline nature of the composite sample can be seen from the ring pattern observed in SAED, as shown in the inset of Figure 2f.

### 3. Thermoelectric Properties

#### 3.1. Electrical Transport

Thermoelectric parameters such as Seebeck coefficient ( $S$ ) and electrical conductivity ( $\sigma$ ) have been measured for all the compositions of STN + MXene in the temperature range of 300 to 950 K. Seebeck coefficient is found to be increased monotonically with temperature for all the compositions, demonstrating degenerate semiconductor like behavior, as shown in Figure 3a. Negative values of  $S$  indicate that electrons are the dominant charge carriers in these oxide composites. Interestingly, thermopower values are not significantly reduced due to the incorporation of conductive 2D MXene in the STN matrix. However, the changes in the electrical conductivity of these composites are more prominent than the change in the Seebeck coefficient, as illustrated in Figure 3b. We have observed 4594% increase in the room temperature electrical conductivity value of the STN + 1 wt% MXene. Maximum electrical conductivity ( $\sigma_{\max}$ ) of  $2.7 \times 10^5 \text{ S m}^{-1}$  at 475 K is attained for 1 wt% MXene incorporation in the STN matrix, which is more than 1851% higher than  $\sigma_{\max}$  obtained for pristine STN, i.e.,  $1.5 \times 10^4 \text{ S m}^{-1}$  at 612 K. Such a remarkable enhancement obtained in the

electrical conductivity of STN + MXene composites without much change in Seebeck coefficient helps us to improve power factor ( $S^2\sigma$ ) by ten times, as shown in Figure 3c. The maximum power factor of over  $3050 \mu\text{W mK}^{-2}$  at 570 K has been obtained for STN + 1 wt% MXene, which is around 1000% larger than that of the pristine STN sample ( $300 \mu\text{W mK}^{-2}$  at 753 K). The cyclability of these composites is further evaluated by collecting thermoelectric data in both a heating and cooling cycle, as shown in Figure S4 (Supporting information). Minimum hysteresis (less than 0.5%) has been found in the heating and cooling cycle data which falls within the instrumental limit implying the viability of these composites for applications at high temperatures (>900 K).

Further, we have estimated the band gap of all the compositions. UV-visible spectroscopy has revealed the effect of MXene addition on the bandgap of composites. Using Kubelka–Munk fitting, it has been found that the band gap of STN + MXene composite is not impacted by the addition of a small concentration (<1%) of MXene, as shown in Figure S5 (Supporting Information) and Table S4 (Supporting Information). However, a higher concentration of MXene ( $\geq 2$  wt%) addition reduces the band gap of STN slightly. Hence, the band model could not describe such remarkable increase in electrical conductivity observed for STN + MXene composites. To understand the surge in electrical conductivity values and unchanged Seebeck coefficient, we have further estimated the electron concentration, mobility, and effective mass of all the compositions. Carrier concentration ( $n$ ) and mobility ( $\mu$ ) of STN + MXene composites have been estimated using Hall measurement, as presented in Table S5 (Supporting Information). The electron

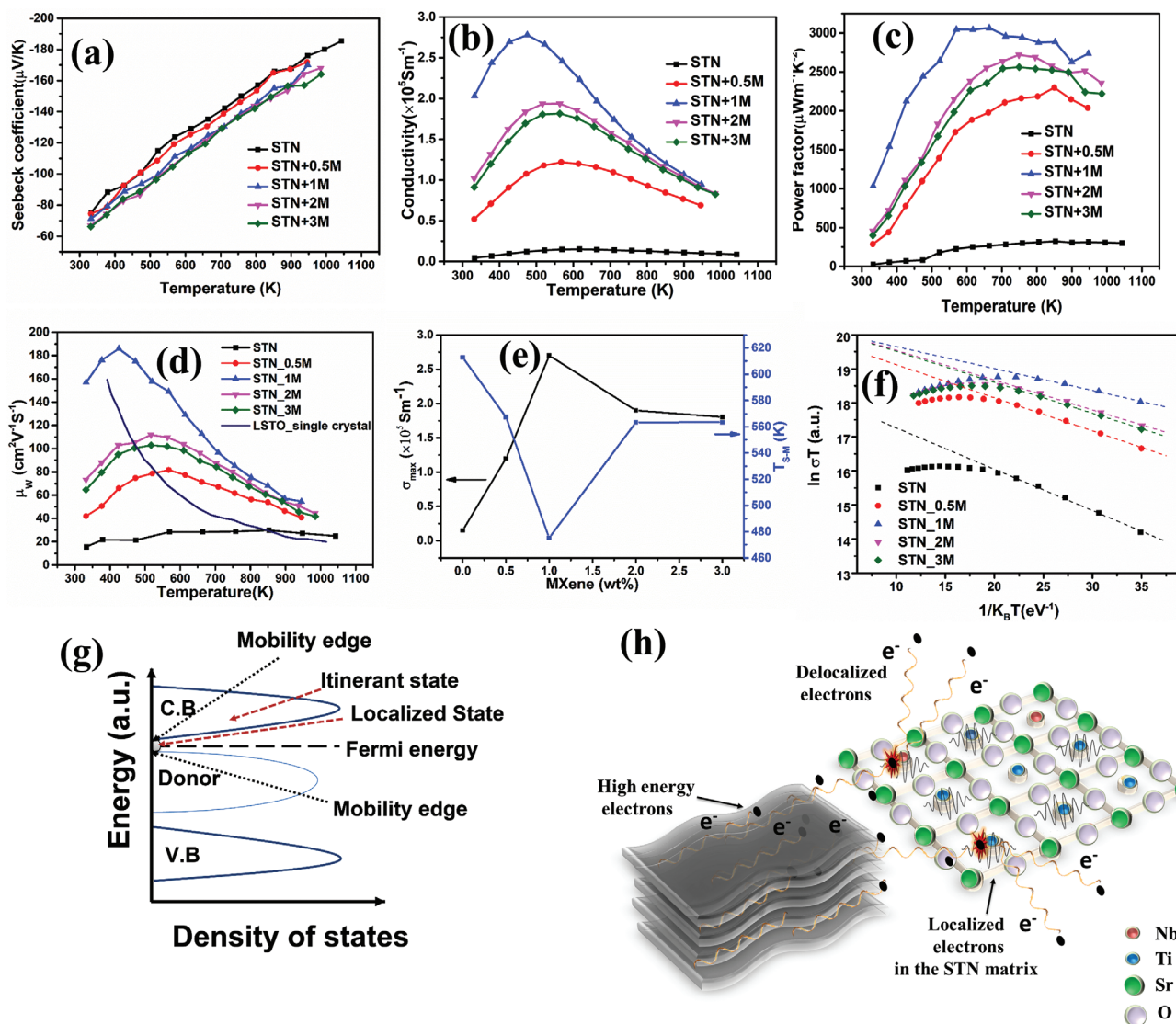


**Figure 3.** Electrical properties: a) Seebeck coefficient, b) electrical conductivity, c) power factor ( $S^2\sigma$ ), d) weighted mobility, e) change in maximum electrical conductivity ( $\sigma_{max}$ ) and semiconductor-to-metal transition temperature ( $T_{S-M}$ ) with the fraction of MXene (wt%) in the STN matrix. f)  $\ln(\sigma T)$  versus  $1/k_B T$  fitted plot showing small polaron hopping in the STN +  $x$  wt% MXene ( $0 \leq x \leq 3$ ) composites. g) Proposed density of states for STN + MXene composite. h) Schematically showing MXene facilitating the delocalization of electrons in the STN matrix by imparting strain and providing high energy electrons.

concentration of all the compositions is found to be in the range  $(4.1 - 5.5) \times 10^{20} \text{ cm}^{-3}$  implying little effect on STN due to incorporation of small amount of MXene. Intriguingly, maximum conductivity is obtained for STN + 1 wt% MXene composite, which does not show any significant change in bandgap and carrier concentration compared to pure STN suggesting that electron transport in these composites is dominated by electron mobility. Moreover, the metal-like temperature-dependent Seebeck coefficient with little effect due to MXene incorporation observed in these composites suggests that carrier concentration remained almost unchanged, and the transport is dominated by mobility. Electron mobility of the composites has been calculated from Hall measurement data as shown in Table S5 (Supporting information). It can be seen that room temperature electron mobility ( $\mu$ ) is increased by order of magnitude

for composite samples compared to that of pristine STN. Maximum mobility is obtained for composite with 1 wt% MXene which demonstrates the maximum conductivity. The density of states effective mass for all the composites has been estimated using the Pisarenko relation (Equation (1))

$$S = \frac{8\pi^2 K_B^2}{3eh^2} m^* T \left( \frac{\pi}{3n} \right)^{\frac{2}{3}} \quad (1)$$

The effective mass of STN, as presented in Figure S6 and Table S5 (Supporting Information), does not change much with the addition of MXene and it remains in the range between  $1.2m_e$  and  $1.34m_e$  for all the compositions. This corroborates well with our observation of the little change in Seebeck coefficient. Since carrier mobility,  $\mu = \frac{e\tau}{m^*}$ , where  $\tau$

is the relaxation time; it can be concluded from little change in effective mass that incorporation of MXene in STN matrix facilitates in smoother charge transport resulting in higher relaxation time which can hardly be explained by conventional band-model.

Further, weighted mobility ( $\mu_w$ ) of electrons, stated by the following Equation (2),<sup>[51,52]</sup> is thought to be a superior descriptor for comprehending the electron-transport phenomena

$$\mu_w = \mu_o \left( \frac{m^*}{m_e} \right)^{\frac{3}{2}} \quad (2)$$

where  $m_e$  is the mass of electrons and  $\mu_o$  is the drift velocity. Equation (2) clearly shows that  $\mu_w$  is independent of carrier concentration. Equation (3)<sup>[51]</sup> has been used to get the weighted mobility of the samples using the Seebeck coefficient and electrical conductivity values

$$\mu_w = \frac{3h^3\sigma}{8\pi\epsilon(2Tk_B m_e)^{\frac{3}{2}}} \times \left[ \frac{\exp\left[\frac{|S|}{k_B} - 2\right]}{1 + \exp\left[-5\left(\frac{|S|}{k_B/e} - 1\right)\right]} + \frac{\frac{3}{\pi^2} \frac{|S|}{k_B/e}}{1 + \exp\left[5\left(\frac{|S|}{k_B/e} - 1\right)\right]} \right] \quad (3)$$

It is evident from Figure 3d that the composites exhibit approximately ten times higher  $\mu_w$  than the pristine STN in the entire temperature range. The mobility of these composites is found to be increased with temperature initially, demonstrating thermally activated charge transport, before it shows decreasing trend corresponding to metal-like electrical transport because of electron scattering by acoustic phonons. On comparing  $\mu_w$  of STN + MXene composites with La or Nb-doped STO single-crystal value,<sup>[23,53]</sup> in Figure 3d, it is evident that our composites exhibit better electron mobility than that of single crystal especially above the semiconductor to metal transition temperature ( $T_{S-M}$ ). A similar phenomenon of enhanced weighted mobility has been observed for graphene-incorporated doped STO samples,<sup>[19]</sup> and Schottky barrier height reduction has been attributed to the enhanced  $\mu_w$ . Unlike graphene, which precipitates along grain boundaries,<sup>[10,11,21]</sup> MXene has been found to form nm to submicron-sized grains. Besides, our XPS data suggest minimal amount of unsaturated -C- bonds present in MXene, unlike graphene. Hence, MXene is not expected to create a similar kind of reducing environment like graphene in STN ceramics. Therefore, we cannot conclude that the Schottky barrier height reduction is solely responsible for the astounding improvement (18.5-fold) in the electrical conductivity values observed in these composites. In complex oxides like STN, where multivalent Ti and Nb ions are present in addition to oxygen vacancies, charge carrier localization phenomena are expected to suppress the electrical conductivity. Hence, the simple band model fails to explain the charge transport mechanism in STN. Interestingly, the carrier concentration of  $10^{20} \text{ cm}^{-3}$  has been found for STN + MXene composites, which

exceeds the critical concentration required to satisfy Mott criteria<sup>[26,54-56]</sup> as depicted by Equation (4)

$$a_B n^{\frac{1}{3}} \approx 0.25 \quad (4)$$

where  $a_B$  is a Bohr radius and  $n$  is a critical carrier concentration. Despite satisfying Mott criteria, it has been observed that STN + MXene nanocomposites show semiconductor-like behavior in lower-temperature regions. However, all the compositions undergo a semiconductor ( $d\sigma/dt > 0$ ) to metal-like ( $d\sigma/dt < 0$ ) transition between 400 and 600 K. Anderson localization<sup>[57-59]</sup> can better explain this behavior as reported in several perovskite oxides.<sup>[26,29,56]</sup> Charge carriers are possibly localized in the mobility edge, as shown in Figure 3g, due to local strain and variable electric fields arising from point defects present in the system. Presence of multivalent cations ( $\text{Nb}^{+5}/\text{Nb}^{+4}$ ,  $\text{Ti}^{+4}/\text{Ti}^{+3}$ ) and oxygen vacancies formed during the heat treatment of STN in a reducing environment generates lattice distortion and a variable local electric field around the point defect centers, leading to the localization of charge carriers called Anderson's transition. Figure 3g depicts that Fermi energy ( $E_F$ ) is located near the conduction band in STN, which consists of localized states, indicated by a gray circle, and is separated from the conduction band by a mobility edge. The present work hypothesizes that introduction of MXene in STN matrix helps these trapped electrons to become delocalized. The role of MXene in delocalizing the electrons can be better comprehended from the plot of  $T_{S-M}$ , semiconductor-to-metal transition temperature and maximum electrical conductivity ( $\sigma_{\text{Max}}$ ) as shown in Figure 3e and Table S6 (Supporting Information). It can be observed that the maximum conductivity value is achieved, when  $T_{S-M}$  is lowest suggesting that MXene incorporation helps in shifting S-M transition of STN enabling it to attain the metallic state at lower temperatures with increased conductivity. The shift in S-M transition temperature ( $T_{S,M}$ ) has been commonly reported in rare earth nickelates ( $\text{RNiO}_3$ ) by various researchers<sup>[42,60,61]</sup> attributing to the lattice strain mismatch. In our composites, MXene has much higher "c" lattice parameter (15.13 Å) than that of STN (3.93 Å) as shown in Table S6 (Supporting Information). In analogy with nickel-based perovskites, the shift in  $T_{S-M}$  of STN + MXene composites can be explained by mismatch in the lattice parameter of MXene and STN matrix. Although we need further theoretical and experimental evidences to fully understand such shift in  $T_{S-M}$ , it is plausible that introduction of MXene imparts enough strain in the STN matrix to aid the localized electrons in attaining the itinerant state enabling it to become metallic at lower temperature, very similar to what has been observed for nickelates. Furthermore, 2D MXene sheets are highly conductive. So, electrons coming out of MXene attain much higher momentum. When these high-energy electrons are injected into the STN matrix, some of their energy gets transferred to the Anderson localized electrons, which move above the mobility edge to attain the itinerant states as schematically shown in Figure 3h. As a result, a massive surge in electrical conductivity is found in STN + MXene composites.

Further, thermally activated charge transport characteristic in the semiconductor region has been explained by the small

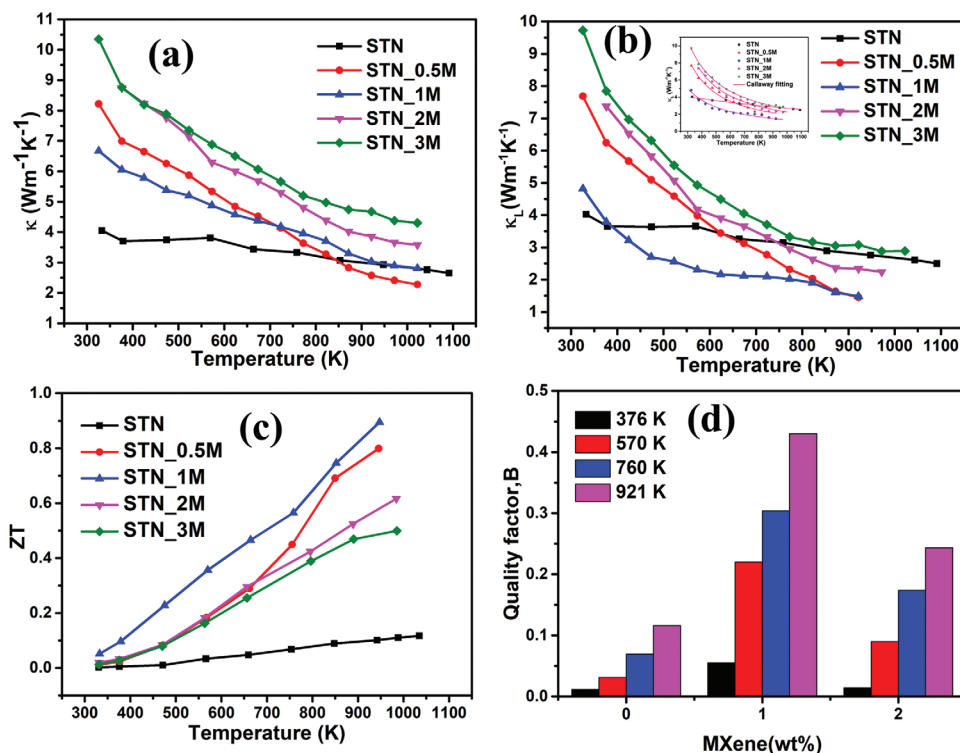


**Figure 4.** Thermal properties and quality factor analysis, plot of change in a) thermal conductivity with temperature, b) lattice thermal conductivity with temperature and the Debye Callaway model fitting for all the composites in the inset. c) Change in ZT with temperature. d) Quality factor of pure STN and composite samples at different temperatures.

polaron hopping (SPH) conduction mechanism. Equation (5) demonstrates the fitted graph for conductivity data using an SPH<sup>[62,63]</sup> model, as shown in Figure 3f

$$\sigma = \frac{\sigma_0}{T} \exp\left(\frac{-E_{\text{hopp}}}{k_B T}\right) \quad (5)$$

here  $E_{\text{hopp}}$  is the activation energy,  $T$  is the absolute temperature,  $\sigma_0$  is a constant, and  $k_B$  is the Boltzmann constant. It is evident that the SPH model controls the thermally activated conduction process in the semiconductor regime of STN + MXene composites. Table S8 (Supporting information) shows that the activation energy required for SPH decreases for the MXene-reinforced STN composites compared to pristine STN, which corroborates well with the enhanced electrical conductivity found in these composites.

### 3.2. Thermal Transport

The thermal conductivity in **Figure 4a** of all the compositions has been computed using Equation (6)

$$\kappa = \rho C_p D \quad (6)$$

where  $\rho$  is the density,  $C_p$  is the specific heat capacity, and  $D$  is the thermal diffusivity. Figure S7a,b (Supporting Information) shows the change in the  $C_p$  and  $D$  with temperature for all the compositions. Thermal conductivity is found to be increased

due to incorporation of MXene in the STN matrix, which was somewhat expected as MXene possesses a high thermal conductivity. However, we have not noticed a significant increase in the thermal conductivities of STN + MXene composites compared to the huge surge in electrical conductivity obtained in these composites due to the presence of highly conductive MXene. Interesting feature of thermal conductivity graph of composites is the steep fall observed with increasing temperature compared to that of pristine STN. Thermal conductivity is a combination of lattice thermal conductivity ( $\kappa_L$ ) and electronic thermal conductivity ( $\kappa_e$ ). The electronic contribution of thermal conductivity is further determined using the Wiedemann Franz law in Equation (7)

$$\kappa_e = L\sigma T \quad (7)$$

where  $L$  stands for the Lorenz number, as shown in Figure S7c (Supporting Information).  $\kappa_e$  has been found to be a replica of the electrical conductivity curve, as depicted in Figure S7d (Supporting Information). However, the overall thermal conductivity does not follow the curvature of  $\kappa_e$  implying the dominance of phonon transport, which is further evaluated by estimating lattice thermal conductivity using Equation (8)

$$\kappa_L = \kappa - \kappa_e \quad (8)$$

Temperature-dependent lattice thermal conductivity ( $\kappa_L$  vs  $T$ ) of all the composites in Figure 4b is higher than pristine STN near 330 K due to the addition of thermally conductive MXene



in the oxide matrix before it exhibits a decreasing trend higher slope with the temperature rise, suggesting the dominance of phonon–phonon Umklapp scattering. We further employed the Debye Callaway model<sup>[64]</sup> stated by Equation (9), to investigate the heat transport mechanism in these composites

$$\kappa_L = \frac{k_B}{2\nu_m\pi^2} \left(\frac{k_B T}{\hbar}\right)^3 \int_0^{\theta_D/T} \frac{\tau(\gamma, T) \gamma^4 e^\gamma}{(e^\gamma - 1)^2} d\gamma \quad (9)$$

where  $\gamma = \hbar \omega / k_B T$  where  $\omega$  is the phonon frequency,  $\hbar$  is the reduced Plank constant,  $\theta_D$  is the Debye temperature,  $\nu_m$  is the mean acoustic velocity, and  $\tau$  is the relaxation time. Relaxation time can be represented by Equation (10)

$$\tau^{-1} = \tau_B^{-1} + \tau_{PD}^{-1} + \tau_U^{-1} + \tau_{ep}^{-1} \quad (10)$$

The above expression demonstrates that  $\tau$  has a contribution from grain boundary scattering ( $\tau_B$ ), point defect scattering ( $\tau_{PD}$ ), phonon–phonon Umklapp scattering ( $\tau_U$ ), and electron–phonon scattering ( $\tau_{ep}$ )

$$\tau^{-1} = \frac{\vartheta_m}{L} + A\omega^4 + B T \omega^2 \exp\left(\frac{\theta_D}{nT}\right) + C\omega^2 \quad (11)$$

where  $L$  is the average grain size,  $A$ ,  $B$ , and  $C$  are fitting parameters related to the point defect, Umklapp scattering, and electron–phonon scattering, respectively. We determined Debye temperature ( $\theta_D$ ) with the help of mean acoustic velocity, as discussed in Table S9 (Supporting Information). According to Casimir,<sup>[65]</sup> grain boundary scattering has not been considered as it is only observed at very low temperatures, and we also omitted the normal scattering process due to point defects, as their contribution is minimal. Figure 4b inset demonstrates a good fit of the Debye Callaway model to our lattice thermal conductivity data. Table S10 (Supporting Information) shows that  $B$  parameter, the measure of Umklapp scattering, is enhanced by three to four times for 0.5 and 1 wt% MXene + STN than that of pristine STN, suggesting enhanced phonon–phonon scattering in the composites. MXene–STN interfaces and stacked layer structure of MXene itself act as phonon scattering centers. The highest value of  $B$  for 1 wt% MXene shows that phonon–phonon scattering is maximum for that composition, and so the lattice thermal conductivity is found to be lower than the pristine STN sample for  $T > 400$  K. A further increase in the MXene concentration results in the formation of agglomerates, reducing the effect of phonon–phonon scattering and increased lattice thermal conductivity ( $\kappa_L$ ). Table S10 (Supporting Information) also depicts that fitting parameter  $C$  decreases with the addition of MXene in STN matrix, inferring the reduced effect of the electron–phonon scattering mechanism on the  $\kappa_L$  of the system. It is vital to notice that even though high electrical conductivity values contribute a considerable increase in  $\kappa_e$ , we were still able to check the overall thermal conductivity by lowering the values of  $\kappa_L$  at higher temperatures. Similar to several studies<sup>[12,14,15]</sup> depicting multifold reductions in  $\kappa_L$  in graphene-doped SrTiO<sub>3</sub>, it is apparent that MXene could introduce anharmonicity in the STN matrix enabling the enhanced phonon scattering in the STN + MXene composites.

As demonstrated in Figure S7e (Supporting information), the addition of MXene to the STN matrix results in almost two orders of magnitude increase in the ratio of electrical to thermal conductivity ( $\sigma/\kappa$ ) at both ambient temperature and 921 K. As a result, we have achieved a more than 700% increase in the  $ZT$  value of STN + MXene composites. Figure 4c shows that the STN + 1 wt% MXene composite exhibits a maximum  $ZT$  of 0.9 at 921 K, which is approximately nine times greater than that of pure STN. Additionally, we computed the dimensionless thermoelectric quality factor “ $B$ ” using the following Equation (12)<sup>[66]</sup> to quantify the impact of MXene inclusion in the STN matrix

$$B = \left(\frac{k_B}{e}\right)^2 \frac{8\pi e (2m_e k_B T)^{3/2} \mu_w}{3h^3 k_L} T \quad (12)$$

The  $B$  values at various temperatures and varying MXene content (0.5, 1, 2 wt%) are shown in Figure 4d. Likewise, Selenide and Telluride-based thermoelectric<sup>[67–69]</sup> materials, STN + 1 wt% MXene, demonstrates a considerable increase in  $B$  value at 921 K compared to pure STN.<sup>[69,70]</sup> The greater  $\mu_w$  and reduced  $\kappa_L$  values at a higher temperature are the causes of the sharp rise in the  $B$  value for the STN-MXene composite.

### 3.3. Efficiency Calculation

The maximum efficiency of a thermoelectric material has been calculated using Equation (13)<sup>[71]</sup>

$$\eta_{max} = \eta_c \frac{(\sqrt{1 + ZT_{avg}}) - 1}{(\sqrt{1 + ZT_{avg}}) + T_c/T_h} \quad (13)$$

where  $Z$  is the figure of merit at average temperature ( $T_{avg}$ ) and  $\eta_c$  is the Carnot efficiency. The cold and hot end temperatures are  $T_c$  and  $T_h$ , respectively. Using the aforementioned formula, 14% efficiency has been obtained for STN + 1 wt% MXene composite. Further, we have conducted finite element modeling (FEM) to determine their power output and efficiency. Using COMSOL Multiphysics, a 3D model of 3 mm × 3 mm × 8 mm TE leg made of STN + 1 wt% MXene composite has been constructed, keeping the cold and hot ends fixed at 300 and 1000 K, respectively, as shown in Figure S8 (Supporting Information). Based on our FEM, the n-type thermoelectric module made of STN + MXene composite alone can produce a power output density of 52.6 kW m<sup>-2</sup> using the input heat flux of 0.55 MW m<sup>-2</sup>. It infers that STN + MXene composite can convert MW-level high-grade waste-heat produced above 900 K into kW-level electricity, which makes this material for application in scavenging the high-temperature waste heat abundantly found in manufacturing industries.

### 3.4. Device Fabrication

Further, to evaluate the potential for generating electricity, a four-legged (3 mm × 3 mm × 8 mm) n-type thermoelectric device or TEG of STN + 1 wt% MXene composite

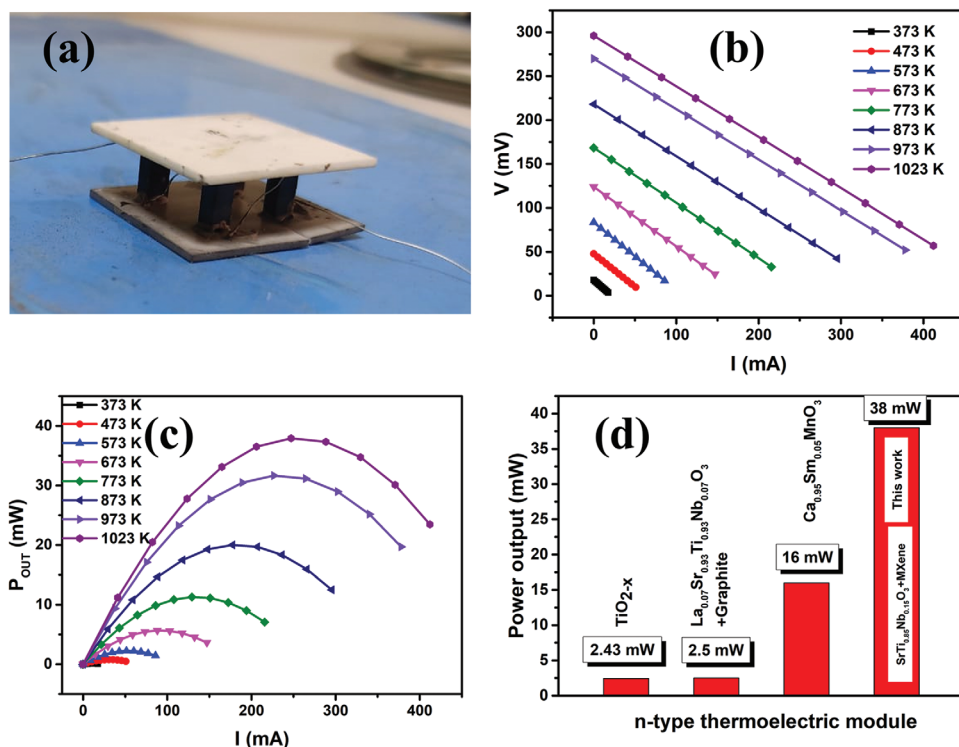


**Figure 5.** a) Prototype of four-legged TEG made of n-type STN + 1 wt% MXene. b)  $I$ - $V$  curve and c) the power output of TEG at different temperatures. d) Comparison of maximum power output obtained in the current work with various n-type oxide thermoelectric devices reported in the literature, such as TiO<sub>2-x</sub>,<sup>[43]</sup> La<sub>0.07</sub>Sr<sub>0.93</sub>Ti<sub>0.93</sub>Nb<sub>0.07</sub>O<sub>3</sub> + graphite,<sup>[9]</sup> Ca<sub>0.95</sub>Sm<sub>0.05</sub>MnO<sub>3</sub>.<sup>[45]</sup>

has been fabricated as shown in Figure 5a. Thermoelectric legs are sandwiched between two Al<sub>2</sub>O<sub>3</sub> plates (1 mm × 20 mm × 20 mm). To make electronic connection in series, 0.1 mm thick Ag wire is connected with the n-type thermoelectric legs using high-purity silver paste. Owing to the n-type single-leg configuration, silver wire spans from the top of one leg to the bottom of another. During the measurement, the cold side of the device was kept at 300 K, and the hot side temperature was varied between 373 and 1023 K. Figure 5b,c depicts the measured current, voltage, and power output values. We have obtained the maximum circuit voltage of 296 mV and maximum power output ( $P_{out}$ ) of 38 mW, at a temperature difference of 713 K between hot and cold ends. The maximum power output of our device is further compared with the other published n-type oxide TEGs, as shown in Figure 5d. It can be seen that we have enhanced the maximum power output more than twice the highest-ever power output reported for oxide TEG.<sup>[45]</sup> It is anticipated that power output can be further increased by combining p-type oxide thermoelectric and fabricating large TEG with optimized device parameters. As shown in Figure S10 (Supporting Information), maximum power of 38 mW, which we obtained from our only prototype comprising only n-type TE module, is higher than the maximum power output of 34.4 mW reported for oxide TEG comprising both n-p-type thermoelectric legs. It suggests the huge potential for further improvement of TEG performances using n-type STN + MXene in conjunction with good p-type thermoelectric material.

## 4. Conclusion

In summary, the fabrication of MXene-implanted Nb-doped SrTiO<sub>3</sub> (STN) oxide thermoelectric has resulted in an immense rise in the electrical conductivity values without a significant change in the Seebeck coefficient and thermal conductivity data. Charge transport in these n-type STN + MXene composites is found to be dominated by electron mobility. Submicron-sized MXene grains present in the STN matrix infuse high-energy electrons, which facilitates the delocalization process of the Anderson localized electrons in the oxide perovskites. As a result, better than single-crystal-like electron mobility is observed in these polycrystalline composites above semiconductor to metal transition temperature ( $T_{S-M}$ ), causing an 18.5-fold increase in the electrical conductivity of STN + 1 wt% MXene composite. Analyzing the heat transport mechanism of these composites using the Debye Callaway model infers that dominant Umklapp scattering caused by anharmonicity due to the incorporation of MXene in the STN matrix is responsible for a decrease in lattice thermal conductivity of STN at high temperatures. Maximum  $ZT \approx 0.9$  obtained for STN + MXene composite is 700% enhancement compared to pristine STN.

Further, we have obtained the highest ever reported power output of 38 mW in the prototype of TEG fabricated using only n-type STN + MXene composite. Our FEM implies the capability of STN + MXene to generate kW-level electricity from MW-level high-grade waste heat. It is reckoned that the performance of TEG can be further improved by assembling

our n-type thermoelectric modules with compatible high-ZT p-type thermoelectrics along with optimization of various device parameters. Our result suggests the huge potential for utilizing oxide perovskite-based TEG in manufacturing industries, thermal power plants (e.g., turbine, chimney), and automobile industries for high-temperature (above 900 K) waste heat recovery.

## Supporting Information

Supporting Information is available from the Wiley Online Library or from the author.

## Acknowledgements

This work was supported by the grant from Science and Engineering Research Board, DST (SERB-DST), India (grant no: IMP/2018/000955).

## Conflict of Interest

The authors declare no conflict of interest.

## Author Contributions

T.M. was responsible for the original research concept and physical interpretation. P.D. synthesized the composite samples and performed all the experiments. S.J. synthesized STN powder. P.D. analyzed the data with the help of T.M. P.D. wrote the main manuscript with the help of T.M. T.M. and P.D. filed an Indian patent (#202111061389) based on the work reported in this paper.

## Data Availability Statement

The data that support the findings of this study are available from the corresponding author upon reasonable request.

## Keywords

doped SrTiO<sub>3</sub>, MXene, oxide thermoelectrics, perovskites

Received: October 31, 2022

Revised: February 8, 2023

Published online:

- [1] G. Y. Zhao, Z. Y. Liu, Y. He, H. J. Cao, Y. B. Guo, *Energy* **2017**, *133*, 142.
- [2] A. S. Rattner, S. Garimella, *Energy* **2011**, *36*, 6172.
- [3] N. V. Burnete, F. Mariasiu, C. Depcik, I. Barabas, D. Moldovanu, *Prog. Energy Combust. Sci.* **2022**, *91*, 101009.
- [4] G. Tan, L.-D. Zhao, M. G. Kanatzidis, *Chem. Rev.* **2016**, *116*, 12123.
- [5] J. Wang, B.-Y. Zhang, H.-J. Kang, Y. Li, X. Yaer, J.-F. Li, Q. Tan, S. Zhang, G.-H. Fan, C.-Y. Liu, *Nano Energy* **2017**, *35*, 387.
- [6] M. T. Dylla, J. J. Kuo, I. Witting, G. J. Snyder, *Adv. Mater. Interfaces* **2019**, *6*, 1900222.
- [7] H. Mun, S. Choi, K. H. Lee, S. W. Kim, *ChemSusChem* **2015**, *8*, 2312.
- [8] M. Acharya, S. S. Jana, M. Ranjan, T. Maiti, *Nano Energy* **2021**, *84*, 105905.
- [9] S. S. Jana, T. Maiti, *ACS Appl. Mater. Interfaces* **2022**, *14*, 14174.
- [10] P. Dey, S. S. Jana, F. Anjum, T. Bhattacharya, T. Maiti, *Appl. Mater. Today* **2020**, *21*, 100869.
- [11] J. U. Rahman, N. Van Du, W. H. Nam, W. H. Shin, K. H. Lee, W.-S. Seo, M. H. Kim, S. Lee, *Sci. Rep.* **2019**, *9*, 8624.
- [12] Y. Lin, C. Norman, D. Srivastava, F. Azough, L. Wang, M. Robbins, K. Simpson, R. Freer, I. A. Kinloch, *ACS Appl. Mater. Interfaces* **2015**, *7*, 15898.
- [13] C. Wu, J. Li, Y. Fan, J. Xing, H. Gu, Z. Zhou, X. Lu, Q. Zhang, L. Wang, W. Jiang, *J. Alloys Compd.* **2019**, *786*, 884.
- [14] O. Okhay, S. Zlotnik, W. Xie, K. Orlinski, M. J. H. Gallo, G. Otero-Irurueta, A. J. S. Fernandes, D. A. Pawlak, A. Weidenkaff, A. Tkach, *Carbon* **2019**, *143*, 215.
- [15] N. Wang, H. Chen, H. He, W. Norimatsu, M. Kusunoki, K. Koumoto, *Sci. Rep.* **2013**, *3*, 3449.
- [16] D. Srivastava, C. Norman, F. Azough, D. Ekren, K. Chen, M. J. Reece, I. A. Kinloch, R. Freer, *J. Mater. Chem. A* **2019**, *7*, 24602.
- [17] D. Srivastava, C. Norman, F. Azough, M. C. Schäfer, E. Guilmeau, R. Freer, *J. Alloys Compd.* **2018**, *731*, 723.
- [18] W. H. Nam, Y. S. Lim, W. Kim, H. K. Seo, K. S. Dae, S. Lee, W.-S. Seo, J. Y. Lee, *Nanoscale* **2017**, *9*, 7830.
- [19] Y. Lin, M. T. Dylla, J. J. Kuo, J. P. Male, I. A. Kinloch, R. Freer, G. J. Snyder, *Adv. Funct. Mater.* **2020**, *30*, 1910079.
- [20] D. Chen, Y. Zhao, Y. Chen, B. Wang, H. Chen, J. Zhou, Z. Liang, *ACS Appl. Mater. Interfaces* **2015**, *7*, 3224.
- [21] X. Feng, Y. Fan, N. Nomura, K. Kikuchi, L. Wang, W. Jiang, A. Kawasaki, *Carbon* **2017**, *112*, 169.
- [22] T. T. Thanh, N. Van Du, J. Bae, S. Y. Choi, T. Ahmed, S. A. Khan, J. Y. Cho, W. H. Nam, D. D. Le, S. Lee, *Solid State Sci.* **2021**, *122*, 106774.
- [23] J. Cao, D. Ekren, Y. Peng, F. Azough, I. A. Kinloch, R. Freer, *ACS Appl. Mater. Interfaces* **2021**, *13*, 11879.
- [24] J. Huang, P. Yan, Y. Liu, J. Xing, H. Gu, Y. Fan, W. Jiang, *ACS Appl. Mater. Interfaces* **2020**, *12*, 52721.
- [25] N. F. Mott, *Proc. Phys. Soc., London, Sect. A* **1949**, *62*, 416.
- [26] A. Biswas, K.-S. Kim, Y. H. Jeong, *J. Appl. Phys.* **2014**, *116*, 213704.
- [27] S. R. Gilbert, L. A. Wills, B. W. Wessels, J. L. Schindler, J. A. Thomas, C. R. Kannewurf, *J. Appl. Phys.* **1996**, *80*, 969.
- [28] P. Roy, V. Waghmare, K. Tanwar, T. Maiti, *Phys. Chem. Chem. Phys.* **2017**, *19*, 5818.
- [29] T. Maiti, M. Saxena, P. Roy, *J. Mater. Res.* **2019**, *34*, 107.
- [30] Y. Li, J. Liu, J.-C. Li, Y.-F. Chen, X.-M. Zhang, X.-J. Wang, F.-N. Wang, W.-B. Su, L.-L. Zhao, C.-L. Wang, *Phys. Chem. Chem. Phys.* **2018**, *20*, 20571.
- [31] G. S. Gund, J. H. Park, R. Harpalsinh, M. Kota, J. H. Shin, T. Kim, Y. Gogotsi, H. S. Park, *Joule* **2019**, *3*, 164.
- [32] O. Mashtalir, M. Naguib, V. N. Mochalin, Y. Dall'Agnese, M. Heon, M. W. Barsoum, Y. Gogotsi, *Nat. Commun.* **2013**, *4*, 1716.
- [33] A. Lipatov, H. Lu, M. Alhabeb, B. Anasori, A. Gruverman, Y. Gogotsi, A. Sinitskii, *Sci. Adv.* **2018**, *4*, eaat0491.
- [34] A. S. Zeraati, S. A. Mirkhani, P. Sun, M. Naguib, P. V. Braun, U. Sundararaj, *Nanoscale* **2021**, *13*, 3572.
- [35] A. Morales-Garcia, F. Calle-Vallejo, F. Illas, *ACS Catal.* **2020**, *10*, 13487.
- [36] F. Dixit, K. Zimmermann, R. Dutta, N. J. Prakash, B. Barbeau, M. Mohseni, B. Kandasubramanian, *J. Hazard. Mater.* **2022**, *423*, 127050.
- [37] J. Ran, G. Gao, F.-T. Li, T.-Y. Ma, A. Du, S.-Z. Qiao, *Nat. Commun.* **2017**, *8*, 13907.
- [38] S. J. Kim, H.-J. Koh, C. E. Ren, O. Kwon, K. Maleski, S.-Y. Cho, B. Anasori, C.-K. Kim, Y.-K. Choi, J. Kim, *ACS Nano* **2018**, *12*, 986.

- [39] J. Liu, H. Zhang, R. Sun, Y. Liu, Z. Liu, A. Zhou, Z. Yu, *Adv. Mater.* **2017**, *29*, 1702367.
- [40] J. Guo, B. Legum, B. Anasori, K. Wang, P. Lelyukh, Y. Gogotsi, C. A. Randall, *Adv. Mater.* **2018**, *30*, 1801846.
- [41] X. Lu, Q. Zhang, J. Liao, H. Chen, Y. Fan, J. Xing, S. Gu, J. Huang, J. Ma, J. Wang, *Adv. Energy Mater.* **2020**, *10*, 1902986.
- [42] N. Palina, L. Wang, S. Dash, X. Yu, M. B. H. Breese, J. Wang, A. Rusydi, *Nanoscale* **2017**, *9*, 6094.
- [43] M. Castañeda, E. I. Gutiérrez-Velásquez, C. E. Aguilar, S. Neves Monteiro, A. A. Amell, H. A. Colorado, *Sustainability* **2022**, *14*, 5987.
- [44] X. Yu, X. Cai, H. Cui, S.-W. Lee, X.-F. Yu, B. Liu, *Nanoscale* **2017**, *9*, 17859.
- [45] S. Lemonnier, C. Goupil, J. Noudem, E. Guilmeau, *J. Appl. Phys.* **2008**, *104*, 014505.
- [46] O. V. Merkulov, D. Lopes, A. A. Markov, N. M. Ferreira, M. V. Patrakeev, A. V. Kovalevsky, *ACS Appl. Energy Mater.* **2021**, *4*, 5848.
- [47] E. S. Reddy, J. G. Noudem, S. Hebert, C. Goupil, *J. Phys. D: Appl. Phys.* **2005**, *38*, 3751.
- [48] W. Shin, N. Murayama, K. Ikeda, S. Sago, *J. Power Sources* **2001**, *103*, 80.
- [49] P. Dixit, T. Maiti, *Ceram. Int.* **2022**, *48*, 36156.
- [50] A. Tkach, J. Resende, K. V. Saravanan, M. E. Costa, P. Diaz-Chao, E. Guilmeau, O. Okhay, P. M. Vilarinho, *ACS Sustainable Chem. Eng.* **2018**, *6*, 15988.
- [51] G. J. Snyder, A. H. Snyder, M. Wood, R. Gurunathan, B. H. Snyder, C. Niu, *Adv. Mater.* **2020**, *32*, 2001537.
- [52] D. M. Rowe, *CRC Handbook of Thermoelectrics*, CRC Press, Boca Raton, FL **2018**.
- [53] S. Ohta, T. Nomura, H. Ohta, K. Koumoto, *J. Appl. Phys.* **2005**, *97*, 034106.
- [54] L. Bjaalie, A. Janotti, B. Himmetoglu, C. G. Van de Walle, *Phys. Rev. B* **2014**, *90*, 195117.
- [55] T. Okuda, K. Nakanishi, S. Miyasaka, Y. Tokura, *Phys. Rev. B* **2001**, *63*, 113104.
- [56] S. Lee, J. A. Bock, S. Trolier-McKinstry, C. A. Randall, *J. Eur. Ceram. Soc.* **2012**, *32*, 3971.
- [57] P. W. Anderson, *Phys. Rev.* **1958**, *109*, 1492.
- [58] P. Bernasconi, I. Biaggio, M. Zgonik, P. Günter, *Phys. Rev. Lett.* **1997**, *78*, 106.
- [59] H. Ihrig, D. Hennings, *Phys. Rev. B* **1978**, *17*, 4593.
- [60] Y. Kumar, R. J. Choudhary, S. K. Sharma, M. Knobel, R. Kumar, *Appl. Phys. Lett.* **2012**, *101*, 132101.
- [61] J. Liu, M. Kareev, D. Meyers, B. Gray, P. Ryan, J. W. Freeland, J. Chakhalian, *Phys. Rev. Lett.* **2012**, *109*, 107402.
- [62] T. Holstein, *Ann. Phys.* **1959**, *8*, 343.
- [63] R. Raffaele, H. U. Anderson, D. M. Sparlin, P. E. Parris, *Phys. Rev. B* **1991**, *43*, 7991.
- [64] J. Callaway, *Phys. Rev.* **1959**, *113*, 1046.
- [65] H. B. G. Casimir, *Physica* **1938**, *5*, 495.
- [66] Y. Pei, H. Wang, G. J. Snyder, *Adv. Mater.* **2012**, *24*, 6125.
- [67] I. T. Witting, J. A. Grovogui, V. P. Dravid, G. J. Snyder, *J. Materiomics* **2020**, *6*, 532.
- [68] Z. Geng, D. Shi, L. Shi, Y. Li, G. J. Snyder, K. Lam, *J. Materiomics* **2019**, *5*, 626.
- [69] P. Jood, J. P. Male, S. Anand, Y. Matsushita, Y. Takagiwa, M. G. Kanatzidis, G. J. Snyder, M. Ohta, *J. Am. Chem. Soc.* **2020**, *142*, 15464.
- [70] I. T. Witting, T. C. Chasapis, F. Ricci, M. Peters, N. A. Heinz, G. Hautier, G. J. Snyder, *Adv. Electron. Mater.* **2019**, *5*, 1800904.
- [71] A. F. Ioffe, L. S. Stil'Bans, E. K. Iordanishvili, T. S. Stavitskaya, A. Gelbtuch, G. Vineyard, *Phys. Today* **1959**, *12*, 42.